

---

This is the **submitted version** of the journal article:

Li, Mengyao; Liu, Yu; Zhang, Yu; [et al.]. «PbS-Pb-Cu xS Composites for Thermoelectric Application». *ACS applied materials & interfaces*, Vol. 13, Num. 43 (October 2021), p. 51373-51382. DOI 10.1021/acsami.1c15609

---

This version is available at <https://ddd.uab.cat/record/275371>

under the terms of the  IN COPYRIGHT license

# PbS-Pb-Cu<sub>x</sub>S Composites for Thermoelectric Application

*Mengyao Li,<sup>†</sup> Yu Liu,<sup>\*,‡,§</sup> Yu Zhang,<sup>†</sup> Xu Han,<sup>⊥</sup> Ke Xiao,<sup>†</sup> Mehran Nabahat,<sup>δ</sup> Jordi Arbiol,<sup>⊥¶</sup> Jordi Llorca,<sup>§</sup> Maria Ibañez,<sup>‡</sup> Andreu Cabot<sup>\*,†,¶</sup>*

<sup>†</sup>Catalonia Energy Research Institute - IREC, Sant Adrià de Besòs, 08930 Barcelona, Spain.

<sup>‡</sup> Institute of Science and Technology Austria (IST Austria), Am Campus 1, 3400, Klosterneuburg, Austria.

<sup>§</sup> School of Chemistry and Chemical Engineering, Hefei University of Technology, Hefei 230009, China.

<sup>⊥</sup> Catalan Institute of Nanoscience and Nanotechnology (ICN2), CSIC and BIST, Campus UAB, Bellaterra, 08193 Barcelona, Catalonia, Spain.

<sup>δ</sup> Department of Physics, Universitat Politècnica de Catalunya. 08930 Barcelona, Spain.

<sup>¶</sup>ICREA, Pg. Lluís Companys 23, 08010 Barcelona, Catalonia, Spain.

<sup>§</sup>Institute of Energy Technologies, Department of Chemical Engineering and Barcelona Research Center in Multiscale Science and Engineering, Universitat Politècnica de Catalunya, EEBE, 08019 Barcelona, Spain

## ABSTRACT

Composite materials offer numerous advantages in a wide range of applications, including thermoelectrics. Here semiconductor-metal composites are produced by just blending nanoparticles of a sulfide semiconductor obtained in aqueous solution and at room temperature, with a metallic Cu powder. The obtained blend is annealed in a reducing atmosphere and afterwards consolidated into dense polycrystalline pellets through spark plasma sintering (SPS). We observe that, during the annealing process, the presence of metallic copper activates a partial reduction of the PbS, resulting in the formation of PbS-Pb-Cu<sub>x</sub>S composites. The presence of metallic lead during the SPS process facilitates the liquid-phase sintering of the composite. Besides, by comparing the transport properties of PbS, the PbS-Pb-Cu<sub>x</sub>S composites, and PbS-Cu<sub>x</sub>S composites obtained by blending PbS and Cu<sub>x</sub>S nanoparticles, we demonstrate that the presence of metallic lead decisively contributes to a strong increase of the charge carrier concentration through spillover of charge carriers enabled by the low work function of lead. The increase in charge carrier concentration translates into much higher electrical conductivities

and moderately lower Seebeck coefficients. These properties translate into power factors up to  $2.1 \text{ mW m}^{-1} \text{ K}^{-2}$  at ambient temperature, well above those of PbS and  $\text{PbS} + \text{Cu}_x\text{S}$ . Additionally, the presence of multiple phases in the final composite results in a notable decrease in the lattice thermal conductivity. Overall, the introduction of metallic copper in the initial blend results in a significant improvement of the thermoelectric performance of PbS, reaching a dimensionless thermoelectric figure of merit  $ZT = 1.1$  at 750 K, which represents about a 400% increase over bare PbS. Besides, an average  $ZT_{ave} = 0.72$  in the temperature range 320-773 K is demonstrated.

**Keywords:** PbS, solution synthesis,  $\text{Cu}_x\text{S}$ , thermoelectric, nanocomposite, nanoparticle, energy conversion.

## 1. Introduction

The energy conversion efficiency of thermoelectric devices strongly depends on three key material properties: Seebeck coefficient ( $S$ ), electrical conductivity ( $\sigma$ ), and thermal conductivity ( $\kappa$ ), which can be grouped within a dimensionless figure of merit:  $ZT = S^2 \sigma T / \kappa$ . Among the numerous strategies used to maximize this thermoelectric figure of merit and thus the device efficiency, the use of composite materials offers numerous advantages.<sup>1-3</sup> In composites, the thermal conductivity can be strongly reduced by effective phonon scattering at the interfaces of two dissimilar materials.<sup>4-9</sup> Additionally, high electrical conductivities can be reached by adjusting the charge carrier concentration with a minor influence on the charge carrier mobility through modulation doping.<sup>10-13</sup> Besides, the Seebeck coefficient can also be increased by selective scattering of minority and low energy charge carriers at interfaces.<sup>14,15</sup>

A particularly interesting type of nanocomposite is obtained from combining a semiconductor host having a large Seebeck coefficient with metallic inclusions of a material providing a proper band alignment with the host. This combination offers a strong acoustic impedance mismatch between the two phases that results in an efficient interface phonon scattering.<sup>16-19</sup> Additionally, metals are convenient charge pools that can adjust the host charge carrier concentration through charge spillover. Besides, metal-semiconductor interfaces can effectively scatter minority and low energy carriers.

PbS is regarded as a paradigmatic thermoelectric material owing to its simple binary composition and excellent charge transport properties.<sup>20-29</sup> Numerous previous works have reported the improvement of the thermoelectric properties of PbS-based materials through doping. We recently demonstrated the possibility of doping PbS with lead halide perovskites.<sup>30</sup> Lou *et al.* reported Ga and In co-doping to modify the PbS conduction band and increase the power factor to reach ZT values up to 1.0 at 923 K for Pb<sub>0.9865</sub>Ga<sub>0.0125</sub>In<sub>0.001</sub>S.<sup>8</sup> Yang *et al.* reported a decrease of the PbS lattice thermal conductivity and a modified energy band configuration by doping with Cl and Sb, reaching ZT up to 1.0 at 823K for PbS-0.0067%PbCl<sub>2</sub>-1.5%Sb.<sup>24</sup> Cheng *et al.* showed Ga doping to result in n-type PbS with higher electrical conductivities, obtaining a ZT of 0.9 at 723 K for Pb<sub>0.99</sub>Ga<sub>0.01</sub>S.<sup>5</sup> Zhao *et al.* reported the properties of n-type PbS-based materials to be enhanced through optimizing the electrical conductivity and thermal conductivity by Cl doping and Bi alloying, reaching a ZT of 0.8 at 823 K for Pb<sub>0.99</sub>Bi<sub>0.01</sub>S-0.067%PbCl<sub>2</sub>.<sup>31</sup> Xiao *et al.* reported Sn alloying in PbS to modify the PbS conduction band and the incorporation of a PbTe phase to decrease the thermal conductivity to reach a high ZT of 1.3 at 923 K for Pb0.94Sn0.06S-8%PbTe.<sup>27</sup> Besides, in a previous publication, we presented experimental results on the thermal and electrical transport properties of PbS-metal composites produced by a versatile particle blending procedure, and where the metal work function allowed injecting electrons to the intrinsic PbS host.<sup>11,12</sup>

In the present work, we present an even more simple strategy to prepare a composite material with improved performance through a slightly more intricate mechanism. The composite material is obtained by blending PbS nanoparticles produced at ambient temperature and atmosphere in aqueous solution with a commercial Cu powder. The powder blend is annealed in a reducing atmosphere to remove surface oxides, and consolidated into dense polycrystalline composites through SPS. Subsequently, the thermoelectric properties of the obtained composites are characterized and compared with those of PbS and a PbS blend with Cu<sub>x</sub>S nanoparticles. Results show the strong and indirect effect of the presence of copper and the processing parameters on the thermoelectric properties of the obtained composites.

## 2. Experimental

**2.1. Chemicals:** Lead (II) acetate trihydrate (Pb(OOCCH<sub>3</sub>)<sub>2</sub>·3H<sub>2</sub>O), copper (II) nitrate

trihydrate ( $\text{Cu}(\text{NO}_3)_2 \cdot 3\text{H}_2\text{O}$ ), and ammonium sulfide solution ( $(\text{NH}_4)_2\text{S}$ , 20% in  $\text{H}_2\text{O}$ ) were purchased from Fisher. Copper powder ( $<45\text{ }\mu\text{m}$ ) was purchased from Sigma. All chemicals were used as received, without further purification.

**2.2. *PbS nanoparticles*:** All reactions were carried out under ambient temperature, pressure and atmosphere in a fume hood. To produce PbS nanoparticles, 5 g  $\text{Pb}(\text{CH}_3\text{COO})_2 \cdot 3\text{H}_2\text{O}$  was dissolved with the help of ultrasounds in 100 ml of deionized water inside a bottle. Then, 5 ml  $(\text{NH}_4)_2\text{S}$  aqueous solution was injected into the lead precursor solution. Upon injection of the  $(\text{NH}_4)_2\text{S}$  solution,  $(\text{NH}_4)_2\text{S}$  stoichiometrically reacted with  $\text{Pb}(\text{CH}_3\text{COO})_2$  resulting in the instantaneous precipitation of PbS nanoparticles. PbS was separated by centrifugation and washed two times with  $\text{H}_2\text{O}$  and two more times with ethanol. The product was finally dried under vacuum for 2 hours at room temperature (Figure S1).

**2.3. *PbS pellets*:** Dense PbS polycrystalline materials were produced in two steps. First, nanoparticles were annealed at 600 °C for 180 min under a reducing gas (95%Ar+5% $\text{H}_2$ ) with a flow rate of 20 mL/min inside a tube furnace. The annealed material was ground into a fine powder with an agate mortar, and loaded into a graphite die within the glovebox before being sintered. The spark plasma sintering (SPS) process was carried out under vacuum, in an AGUS PECS SPS System-Model SPS 210Sx, that applied 45 MPa of pressure and a temperature of 600 °C for 5 min. The consolidated pellets were subsequently stored inside the glovebox. Before performing measurements, the pellets were slightly polished to remove the surface oxide layer.

**2.4. *PbS-Cu composites*:** PbS-Cu composites were produced by blending PbS nanoparticles with commercial Cu powder within ethanol and with the aid of an ultrasonic bath for 30 min. The blend was dried under vacuum at room temperature, annealed under a flow or reducing gas, and finally SPS processed under the conditions detailed above.

**2.5. *PbS-Cu<sub>x</sub>S composites*:** PbS-Cu<sub>x</sub>S composites were obtained by blending PbS nanoparticles with CuS nanoparticles using the same methodology and conditions as used to produce PbS-Cu composites. CuS nanoparticles were obtained by reacting 10 mmol  $\text{Cu}(\text{NO}_3)_2 \cdot 3\text{H}_2\text{O}$  with 2 ml  $(\text{NH}_4)_2\text{S}$  in 35 ml of deionized water at room temperature as reported in our previous work.<sup>32</sup>

**2.6. Structural and chemical characterization:** The relative densities of the compacted pellets were measured by the Archimedes' method. X-ray diffraction (XRD) patterns were measured by a Bruker AXS D8 Advance X-ray diffractometer with Cu-K $\alpha$  radiation ( $\lambda = 1.5406 \text{ \AA}$ ). Scanning electron microscopy (SEM) characterization was carried out in an Auriga Zeiss field emission SEM operated at 5.0 kV. Energy dispersive X-ray spectroscopy (EDX) was carried out with an Oxford spectrometer attached to a Zeiss Auriga SEM at 20.0 kV. Transmission electron microscopy (TEM), scanning TEM (STEM), and high resolution TEM (HRTEM) were carried out under the 200 keV Tecnai F20 field emission microscope. Electron energy loss spectroscopy (EELS) and high-angle annular dark-field (HAADF) STEM were carried out using a Gatan Quantum image filter embedded in the F20 (S)TEM. X-ray photoelectron spectroscopy (XPS) was performed on a Specs system, equipped with a Mg anode XR50 source and a Phoibos 150 MCD-9 detector. XPS data were processed using the CasaXPS software.

**2.7. Thermoelectric properties:** The Seebeck coefficient and resistivity were simultaneously measured under helium atmosphere in an LSR-3 Linseis system. All samples were tested for at least three heating and cooling cycles. Considering the system and measurement accuracy and measurement accuracy, we estimated the measurement error of conductivity and Seebeck coefficient to be about 4%. Combining the uncertainties of the electrical conductivity and the Seebeck coefficient, the uncertainty of the power factor ( $\sigma S^2$ ) is *ca.* 10%. Thermal conductivities were obtained by multiplying the thermal diffusivity ( $\lambda$ ), the constant pressure heat capacity ( $C_p$ ) and the density of the material ( $\rho$ ):  $\kappa_{total} = \lambda C_p \rho$ . Thermal diffusivities were measured by a Xenon Flash Apparatus XFA 600 and a Laser Flash Analyzer LFA 1000, Linseis, which have an estimated error of *ca.* 5 %. Thermal conductivities were calculated by  $\kappa_{total} = \lambda C_p \rho$ , where  $\lambda$  is the thermal diffusivity,  $C_p$  is the heat capacity, and  $\rho$  is the mass density of the specimen. The  $C_p$  value was calculated by the Dulong–Petit limit (3R law). We also measured the temperature-dependent  $C_p$  values of PbS-5%Cu sample as a reference, using a NETZSCH DSC 404 F3 differential scanning calorimeter (DSC) at a heating rate of 10 K/min under a flow of high purity N<sub>2</sub> in Pt-Rh/Al<sub>2</sub>O<sub>3</sub> crucible. Sample densities were measured using the Archimedes' method with a *ca.* 2% error. Consequently, the combined uncertainty for all measurements involved in ZT determination shown in the plot is estimated to be *ca.* 15%. The

Hall charge carrier concentrations ( $n_h$ ) and mobilities ( $\mu_h$ ) were measured by the Van der Pauw method at room temperature under a magnetic field of 0.6 T (ezHEMS, NanoMagnetics). Values provided correspond to the average of 6 measurements and the estimated error is *ca.* 10%.

*2.8. Lattice thermal conductivity ( $\kappa_L$ ) calculation:* We estimated the lattice thermal conductivity ( $\kappa_L$ ) by subtracting the electronic thermal conductivity ( $\kappa_e$ ) from the measured total thermal conductivity ( $\kappa_{total}$ ):  $\kappa_L = \kappa_{total} - \kappa_e$ . The electronic contribution  $\kappa_e$  is directly proportional to the electrical conductivity  $\sigma$  as defined by the Wiedemann-Franz law:  $\kappa_e = L\sigma T$ , where  $L$  is Lorentz number that was calculated from the Seebeck coefficient:  $L=1.5+\exp(-|S|/116)$ , with  $L$  in the units  $10^{-8} \text{ V}^2\text{K}^{-2}$  and  $S$  in  $\mu\text{VK}^{-1}$ , as proposed by Snyder *et al.*<sup>33</sup>

### 3. Results and discussions

#### 3.1. PbS nanoparticles

Quasi-spherical PbS nanoparticles with an average size of 18 nm were produced in aqueous solution, without any surfactant, from the reaction of  $(\text{NH}_4)_2\text{S}$  and  $\text{Pb}(\text{CH}_3\text{COO})_2 \cdot 3\text{H}_2\text{O}$  in air atmosphere and at ambient temperature (Figures 1a and S1). The XRD pattern of the obtained material is consistent with the PbS cubic phase (JCPDS No. 01-077-0244, Figure 1b). Figure 1c shows a representative HRTEM micrograph of the PbS sample, with a detail of the orange squared region and its corresponding power spectrum that confirm the cubic PbS crystalline structure (space group = FM3-M) and allows determining the lattice parameter as  $a=b=c=5.9360 \text{ \AA}$ . Electron energy loss spectroscopy (EELS) elemental composition maps obtained from the red squared region in the high-angle annular dark-field imaging (HAADF)-STEM micrograph shown in Figure 1d demonstrate a uniform distribution of Pb and S through the nanoparticles.

The high resolution Pb 4f XPS spectrum of PbS nanoparticles was properly fitted using four bands. The bands located at 142.4 eV and 137.6 eV corresponded to Pb 4f<sub>5/2</sub> and Pb 4f<sub>7/2</sub> core levels of Pb<sup>2+</sup> cations within a PbS chemical environment.<sup>34</sup> Bands at 142.7 eV and 137.9 eV were associated with the Pb 4f core levels of Pb<sup>2+</sup> within a PbO environment.<sup>28,35</sup> The presence of PbO is related to the partial surface oxidation of the material upon exposure to the ambient atmosphere.<sup>36</sup> The S 2p XPS spectrum of PbS displayed just one peak that was fitted with two

bands located at 162.0 eV and 160.8 eV, and which corresponded to S 2p<sub>1/2</sub> and S 2p<sub>3/2</sub> core levels of S<sup>2-</sup> anions within PbS.<sup>28,34,35</sup>

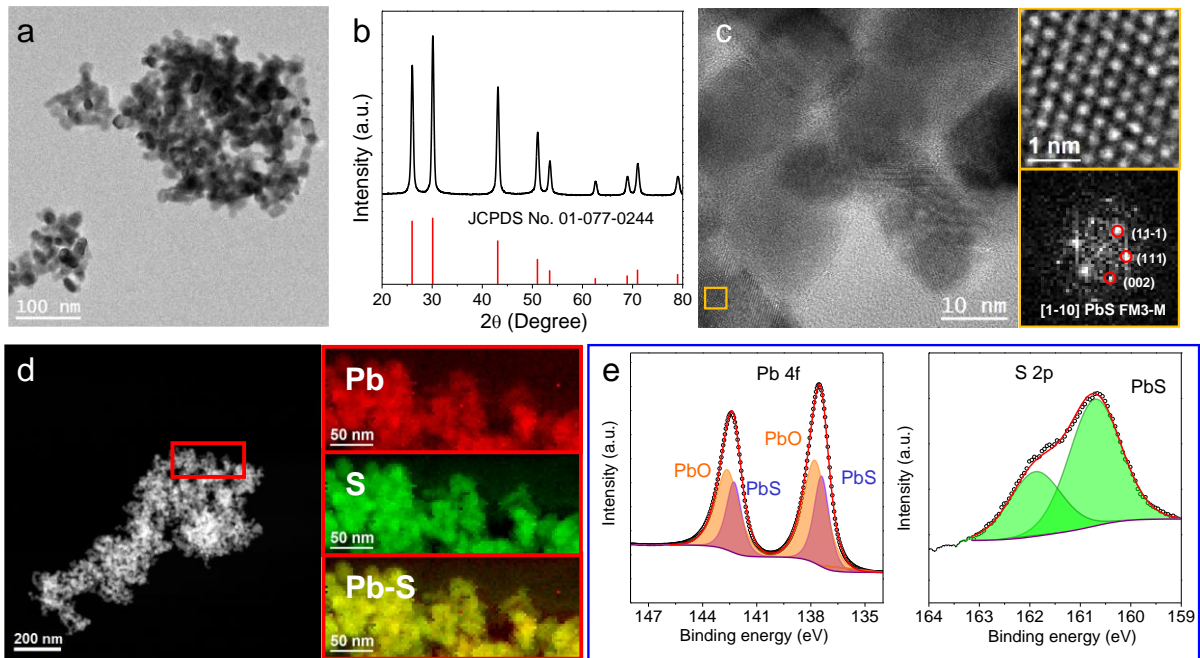


**Figure 1.** Structural and chemical properties of PbS nanoparticles. a) TEM micrograph. b) XRD pattern. c) HRTEM micrograph, detail of the orange squared region and its corresponding power spectrum. From the crystalline domain, the PbS lattice fringe distances were measured to be 0.344 nm, 0.330 nm and 0.296 nm, at 70.39° and 120.78° which could be interpreted as the cubic PbS phase, visualized along its [101] zone axis. d) EELS chemical composition maps obtained from the red squared area in the STEM micrograph. Individual Pb N<sub>4,5</sub>-edge at 413 eV (red), S L<sub>2,3</sub>-edge at 165 eV (green) and its composite. e) Pb 4f and S 2p high resolution XPS spectra.

### 3.2. Thermoelectric properties of PbS

In contrast to PbS, which typically displays an intrinsic n-type behaviour related to the presence of S vacancies, PbO shows p-type conductivity. Thus, the removal of PbO is essential to optimize the thermoelectric properties of PbS-based materials. We removed PbO by annealing the materials in an Ar/H<sub>2</sub> atmosphere at 600 °C for 3 h, as detailed in the experimental section. Figure S2 displays the XRD pattern of the annealed material. Upon annealing, XRD peaks became sharper, indicating a higher crystallinity, and no additional phase was detected.

The annealed material was subsequently loaded into a 10 mm graphite die and spark plasma sintered at 600°C and 45 MPa for 5 min under vacuum. The relative density of the obtained pellet was *ca.* 95% of the theoretical value, as measured by the Archimedes' method. Cross-

section SEM characterization showed the size of the crystal domains within the SPS sintered material to be significantly larger ( $\sim 0.5 \mu\text{m}$ ) than the precursor PbS nanoparticles (Figure S3). To determine the annealing influence on the thermoelectric properties of the materials, a second and third pellet were produced from the SPS of PbS nanoparticles annealed in pure Ar and of unannealed PbS nanoparticles. As expected, the pellet obtained from the annealed PbS displayed a much higher electrical conductivity than the pellet produced from unannealed PbS nanoparticles, especially in the low temperature range (Figure 2). This higher electrical conductivity is related both to the removal of PbO and to the formation of additional S vacancies during the annealing process. The annealing of the material in the presence of  $\text{H}_2$  was demonstrated more effective, resulting in higher electrical conductivities. Both pre-annealed materials displayed negative Seebeck coefficients in all the temperature range measured, denoting n-type conductivity. In contrast, the PbS obtained from unannealed particles was characterized by a positive Seebeck coefficient at temperatures below 500 K and a negative  $S$  at higher temperatures. This change of conductivity type with temperature is consistent with previous works and has been associated with the presence of p-type PbO.<sup>12</sup> When increasing temperature, the concentration of thermally generate charge carriers eventually overcomes the hole density associated with the presence of PbO and the intrinsic n-type character of PbS becomes dominant.

The higher electrical conductivity and absolute Seebeck coefficients of the pre-annealed materials resulted in much higher power factors, up to  $1.1 \text{ mW m}^{-1} \text{ K}^{-2}$ . On the other hand, the smaller crystal domain size of the unannealed material and the presence of an additional phase, PbO, resulted in lower thermal conductivities than those of the pre-annealed PbS.

Overall the material pre-annealed in the presence of  $\text{H}_2$  displayed significantly higher thermoelectric figures of merit than the pellets obtained from the SPS of unannealed PbS nanoparticles and from PbS nanoparticles annealed in pure Ar. Therefore, to investigate the effect of Cu addition, a pre-annealing step was considered for all the samples.

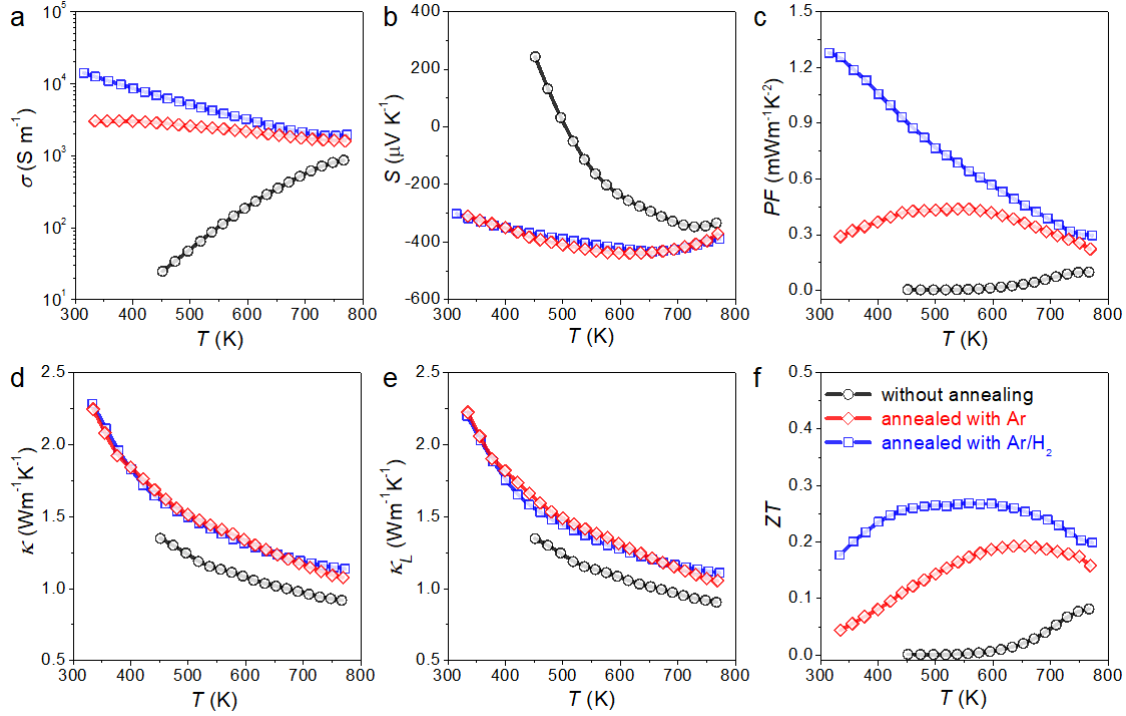


**Figure 2.** Thermoelectric properties of PbS pellets obtained with  $\text{Ar}/\text{H}_2$  (blue), with Ar (red) and without (black) annealing/reduction step: a) electrical conductivity,  $\sigma$ ; b) Seebeck coefficient,  $S$ ; c) power factor,  $PF$ ; d) thermal conductivity,  $\kappa_{total}$ ; e) lattice thermal conductivity,  $\kappa_L$ ; and f) figure of merit,  $ZT$ .

### 3.3. $\text{PbS}+\text{Cu}$

A representative SEM image and the XRD pattern of the commercial Cu particles used to produce PbS+Cu composites are shown in Figure S4. Composites were produced by blending in solution the proper amounts of PbS nanoparticles and the commercial Cu powder, at different Cu molar ratios (0 mol%, 3 mol%, 5 mol%, 7 mol%). The mixture was dried and then annealed in  $\text{Ar}/\text{H}_2$  atmosphere. The XRD patterns of the particle mixture displayed the presence of PbS and metallic copper (Figure 3a). On the other hand, in addition to the fingerprint of the cubic PbS phase, the XRD pattern of the annealed samples did not display the metal copper signal but the diffraction peaks of the metallic Pb phase (Figure 3b). This result indicates that during the hydrogen reduction process, copper reacts with S from PbS, forming metallic Pb and a poor crystallinity  $\text{Cu}_x\text{S}$  phase that is not detected by XRD.

Representative SEM micrographs of the annealed PbS powder and PbS+5%Cu powder are shown in Figure S5. Both materials undergo a clear grain growth during the annealing process.

But the morphology of the two annealed powders is slightly different, with the PbS+Cu sample showing larger grains probably associated with the higher diffusivity of the reduced metallic Pb which contributes to the grain coarsening, as commonly observed in liquid phase sintering processes.<sup>2,37</sup>

The annealed material was ground into a fine powder with an agate mortar, and loaded into a 10 mm graphite die in the glovebox. Then the material was spark plasma sintered at 600°C and 45 MPa for 5 min under vacuum. The relative densities of the consolidated materials were in the range between 92% and 97%, as shown in Table S1. SEM characterization of the PbS+Cu pellets showed their average grain size to be in the micron size range (Figure S3c). Significantly larger grains were observed from the PbS+Cu sample, which results from the sintering of this material in the presence of liquid lead.<sup>37</sup> The XRD patterns of the pellets containing relatively large amounts of Cu displayed the presence of PbS and metallic Pb phases, but no Cu-based phase. XRD patterns displayed no shift of the peaks corresponding to the PbS phase, which denotes a minimal if any incorporation of Cu within the PbS lattice. On the other hand, SEM-EDX elemental maps of the pellets displayed a uniform distribution of S and Pb, with areas containing a higher density of Cu, corresponding to the Cu<sub>x</sub>S domains (Figure S6).

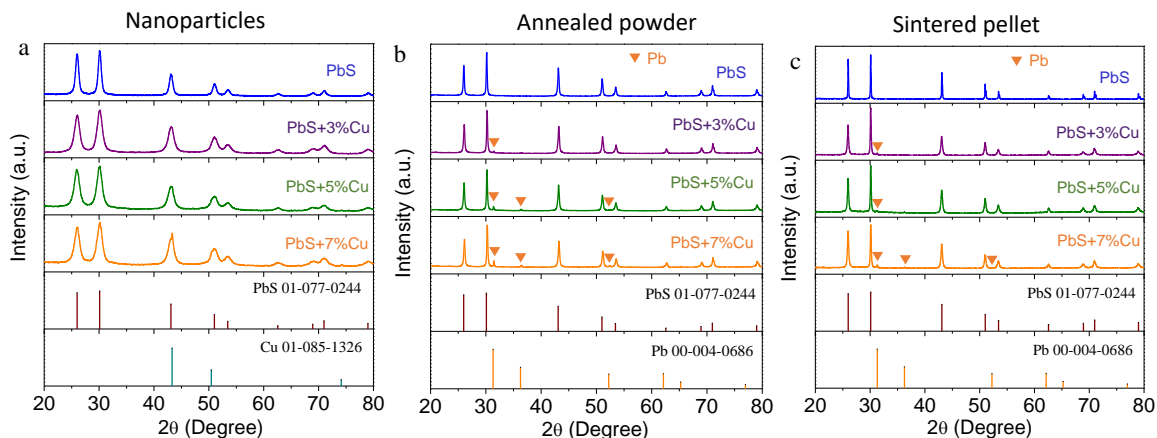


**Figure 3.** XRD patterns of a) PbS + x%Cu nanoparticles, b) annealed powders, and c) SPS sintered pellets.

### 3.4. Thermoelectric properties of PbS+Cu

The aim of combining Cu with PbS was to control the charge carrier concentration of the base

material PbS through charge carrier spillover from metallic Cu domains, which have a relatively low work function (4.7 eV). While Cu<sub>x</sub>S also display low work functions (4.8 eV) and relatively large charge carrier concentrations,<sup>32,38</sup> we selected Cu instead of Cu<sub>x</sub>S because of the higher density of free charges in the metal. However, after a comprehensive analysis of the consolidated material, we observed the PbS+Cu blends to become PbS-Pb-Cu<sub>x</sub>S composites due to the partial reduction of the PbS to Pb and the concomitant oxidation of Cu to Cu<sub>x</sub>S. The redox process occurring during the annealing of the material under Ar+H<sub>2</sub> atmosphere was very convenient for the initial goal of the project because metallic Pb is also characterized by a high charge carrier density than Cu<sub>x</sub>S and at the same time shows an even lower work function (4.14 eV) than metallic Cu.

The PbS-Pb-Cu<sub>x</sub>S composites obtained from the annealing and consolidation of the PbS+Cu blends systematically displayed higher electrical conductivities and lower absolute values of the Seebeck coefficient than PbS (Figure 4), pointing at an increase of the charge carrier concentration with the addition of Cu. Hall measurements quantified the increase of the charge carrier concentration with the presence of Cu in one order of magnitude, from  $1.8 \times 10^{18} \text{ cm}^{-3}$  for PbS to  $1.7 \times 10^{19} \text{ cm}^{-3}$  for PbS+3%Cu (Figure 5a). The increase of the charge carrier concentration is associated with the injection of free electrons from the Pb domains formed during the reduction process in the pellet containing Cu. The charge injection from Pb to PbS domains is enabled by the low work function of Pb and results in a downward band bending at the PbS surface in contact with Pb domains (Figure 5b). Cu<sub>x</sub>S domains could also contribute to the increase of the charge carrier concentration, but we believe Cu<sub>x</sub>S to be less effective when combined with Pb domains owing to the lower position of the Fermi level within Cu<sub>x</sub>S and the lower concentration of free charges in this semiconductor when compared with metallic Pb. We discuss this point further below.

Besides, Hall measurements pointed at a decrease of the charge carrier mobility for the samples containing Cu, which is related to the increase of scattering with the presence of the multiple phases, i.e. Pb and Cu<sub>x</sub>S (Figure 5a).

Based on the single parabolic band (SPB) model, the Seebeck coefficient can be calculated using the following equation:

$$S = \frac{8\pi^2 k_B^2}{3e h^2} m^* T \left( \frac{\pi}{3n_H} \right)^{\frac{2}{3}} \quad (1)$$

where  $k_B$  is the Boltzmann constant,  $h$  is the Planck constant,  $e$  is the elemental charge,  $n_H$  is the charge carrier concentration, and  $m^*$  is the effective mass.<sup>39</sup> Figure 5c,d displays the weighted mobility and the Pisarenko plot including the Seebeck coefficient and charge carrier concentration of all the samples at room temperature. The introduction of copper and the annealing process in a reducing atmosphere indirectly resulted in an increase of the charge carrier concentration by one order of magnitude. Consistently with the above equation, the Seebeck coefficient declined with increasing  $n_H$  (Figure 4b). However, the Seebeck coefficients of the samples containing Cu are slightly above the theoretical curve plotted considering the effective  $m^*$  of PbS, which we associate to a filtering effect that is observed in the form of an increase of the effective mass with the Cu content (Figure 5d). Overall, the adjustment of the Cu concentration and the indirect modulation of  $m^*$  and  $n_H$  allowed reaching very high room temperature power factor, up to  $2.1 \text{ mWm}^{-1}\text{K}^{-2}$  (Figure 4c), which is one of the highest values obtained for PbS-based materials at room temperature (Figure S7a).

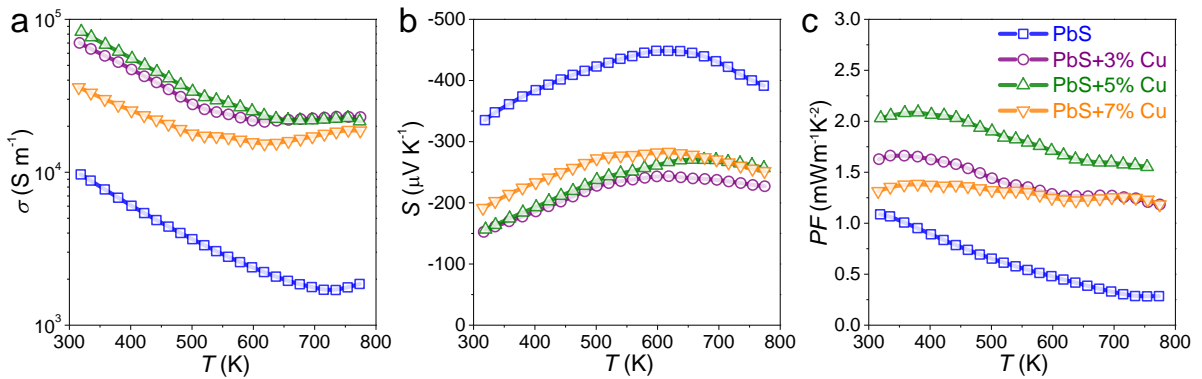


**Figure 4.** Electronic transport properties of PbS+xmol%Cu nanomaterials: a) electrical conductivity,  $\sigma$ ; b) Seebeck coefficient,  $S$ ; c) power factor,  $PF$ .

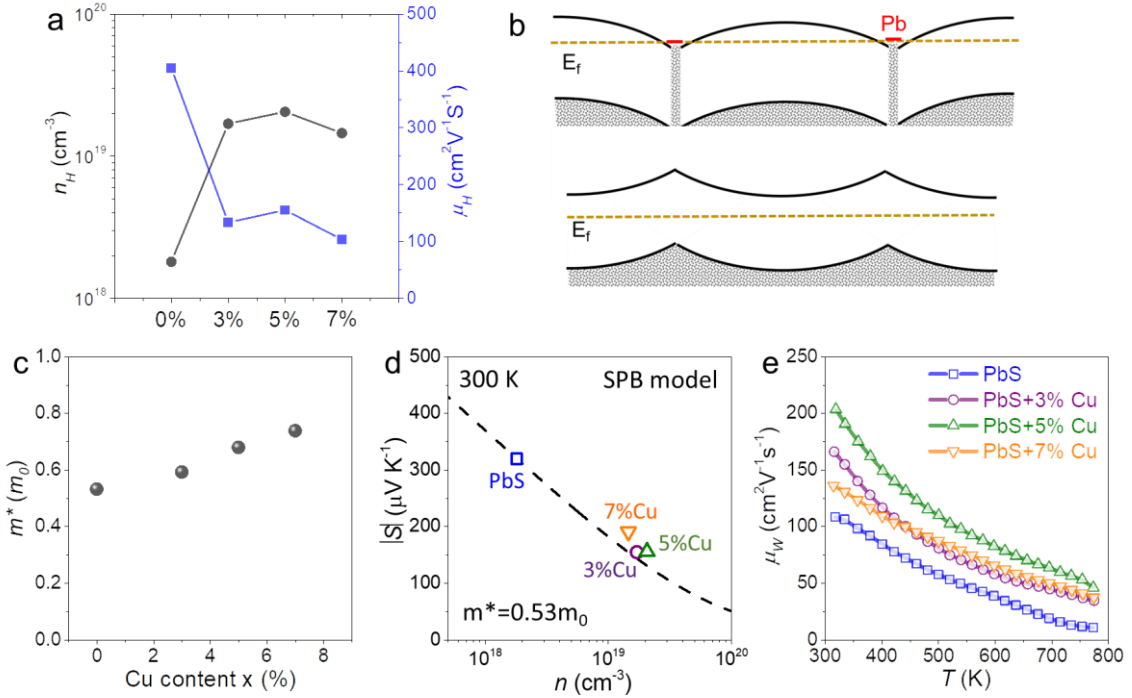


**Figure 5.** a) Hall charge carrier concentration  $n_H$  and mobility  $\mu_H$  of  $\text{PbS} + x$  mol%Cu materials at room temperature. b) Band alignment in pure  $\text{PbS}$  (bottom) and the  $\text{PbS-Pb}$  composite (top). c) Effective mass,  $m^*$ . d) Pisarenko relationship considering the effective mass of  $\text{PbS}$  at room temperature,  $m^* = 0.53 m_0$ . e) Weighted mobility,  $\mu_w$ .

The weighted mobility  $\mu_w$  was calculated from the electrical conductivity and Seebeck coefficient data (Figure 5e):<sup>27,39</sup>

$$\mu_w = \frac{3\sigma}{8\pi e F_0(\eta)} \left( \frac{h^2}{2m_0 k_B T} \right)^{3/2} \quad (2)$$

where  $F_n(\eta)$  is the Fermi integral with  $n=0$  and is defined as:

$$F_n(\eta) = \int_0^\infty \frac{x^n}{1+e^{x-\eta}} dx \quad (3)$$

$$S = \pm \frac{K_B}{e} \left\{ \frac{(r+5/2)F_{r+3/2}(\eta)}{(r+3/2)F_{r+1/2}(\eta)} - \eta \right\} \quad (4)$$

where  $\eta$  is the reduced chemical potential and  $r$  denotes the scattering factor, which we consider as  $r=-1/2$  owing to the dominance of the acoustic scattering mechanism.<sup>40</sup>

We observed  $\mu_w$  to increase with the carrier concentration (Figure 5e), which is in contrast to the decrease of the Hall carrier mobility with the presence of Cu. The enhancement on  $\mu_w$  is

especially significant near room temperature, reaching very high values, up to  $\sim 203 \text{ cm}^2\text{V}^{-1}\text{s}^{-1}$ .

The DSC profile of PbS-Cu samples displayed two feature peaks at about 373 K and 600 K. The feature at 373 K was associated with a phase transition in  $\text{Cu}_x\text{S}$ , further proving the presence of a poorly crystalline  $\text{Cu}_x\text{S}$  phase (Figure S8a). The feature at 600 K was associated with the melting of metallic Pb. The thermal conductivity values obtained using the experimental  $C_p$  values were similar to those obtained from the conventional use of the Dulong-Petit limit (Figures S6 and S9). As expected, the processing of the material in the presence of copper reduced the lattice thermal conductivities ( $\kappa_L = \kappa - \kappa_e$ ) over the entire temperature range (Figure 6). This lower lattice thermal conductivity is related to the enhanced scattering at the interphase of domains with different compositions.

The quality factor  $B$  was calculated using the following equation:<sup>7</sup>

$$B = 9 \frac{\mu W}{k_L} \left( \frac{T}{300} \right)^{5/2} \quad (5)$$

As displayed in Figure 6c,  $B$  increased almost linearly with temperature for all samples and increased with the Cu amount over the entire temperature range.

Overall, the presence of Cu resulted in a very significant increase of  $ZT$  associated with the higher power factors and reduced  $\kappa_{\text{lat}}$ . Record  $ZT$  values were obtained from PbS + 5%Cu samples, reaching  $ZT=1.1$  at 750 K, which is about 4 times higher than that of undoped PbS. Besides, to the best of our knowledge, the  $ZT = 0.28$  obtained at room temperature from PbS + 5%Cu samples, is the highest reported for an n-type PbS-based material (Figure S7b).

A single parabolic band (SPB) model was employed to calculate the  $n$ -dependent  $ZT$  values at 300 K. The experimental  $\kappa_L$  used in the calculations was derived from Figure 6b. Figure S9 displays the comparison of the experimentally achieved figure-of-merit  $ZTs$  with the predicted values. The experiment data are close to the result obtained with the SPB model. The maximum  $ZT$  is obtained at  $n \sim 1.5 \times 10^{19} \text{ cm}^{-3}$  for PbS-5%Cu at 300 K, which is close to our experimental values. Thus, within the framework of the SPB model, the obtained experimental  $ZT \sim 0.28$  at room temperature is very close to the maximum that can be reached in this system. The SPB model in bare PbS follows a similar trend but with a maximum at lower a charge carrier

concentration of *ca.*  $8.6 \times 10^{18} \text{ cm}^{-3}$ .

The PbS + 5%Cu sample was also characterized by a record average ZT in the range from 320 K to 773 K,  $ZT_{avg} = 0.72$  (Figure S7c). Besides, Figure S10 displays the thermoelectric properties of a PbS+5%Cu sample measured for three consecutive temperature cycles, demonstrating excellent stability. It should be noted that the pellet surface oxidizes when exposed to air for a long time, but its high density prevents its bulk oxidation. Thus slightly polishing the surface to be in contact with electrodes is both necessary and also sufficient to recover the performance of the pellets after extended periods exposed to air.

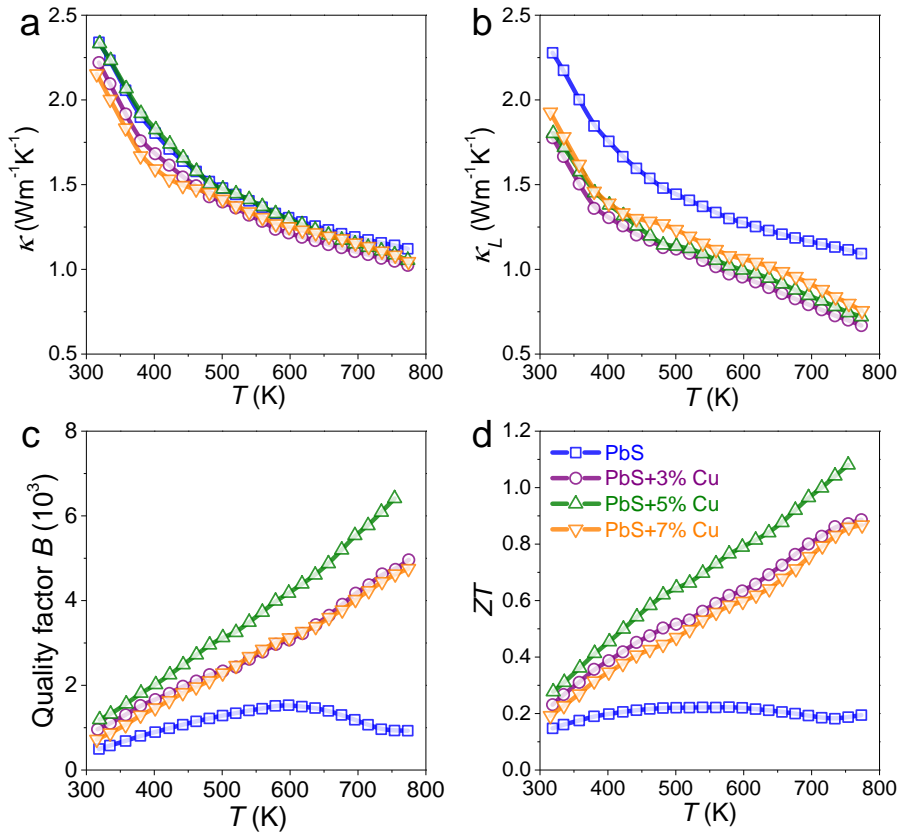


**Figure 6.** a) Thermal conductivity,  $\kappa$ . b) Lattice thermal conductivity,  $\kappa_L$ . c) Quality factor,  $B$ . d) Thermoelectric figure of merit,  $ZT$ .

Finally, to experimentally determine the effect of the metallic Pb and compare it with the effect of  $\text{Cu}_x\text{S}$  domains, we produced and measured a PbS- $\text{Cu}_x\text{S}$  sample, free of metallic Pb, by blending PbS and covellite CuS nanoparticles.<sup>32</sup> As detailed in our previous work, covellite CuS particles lose sulfur during the annealing process, evolving to Cu rich phases such as the tetragonal  $\text{Cu}_{1.96}\text{S}$  and the monoclinic  $\text{Cu}_2\text{S}$  phases (Figure S11), especially in an  $\text{H}_2$  containing

atmosphere.<sup>32,38</sup> Thus, CuS particles are not able to reduce the PbS as occurring in the PbS+Cu blend. Thus, as expected, the annealed PbS+CuS blend displayed no sign of the presence of metallic Pb (Figure S12). Figure 7 displays the thermoelectric properties of the pellets obtained from the annealing and SPS of the PbS+CuS blend, compared with those of PbS and the PbS+Cu pellet. We observe the presence of the Cu<sub>x</sub>S to significantly increase the electrical conductivity as expected from the proper band alignment between Cu<sub>x</sub>S and PbS for the former to inject charge carrier to the latter.<sup>41</sup> However, the electrical conductivities reached in the PbS-Cu<sub>x</sub>S composite were close to a twofold lower than those obtained from PbS-Cu-Cu<sub>x</sub>S pellets with the same amount of Cu. Besides, PbS-Cu<sub>x</sub>S samples were characterized by slightly lower Seebeck coefficients, which could be related to the lack of a filtering effect as described to occur in PbS-Cu-Cu<sub>x</sub>S composites. Overall significantly lower power factors and thermoelectric figures of merit were obtained from composites produced PbS+CuS blends than from PbS+Cu blends (Figure 7).

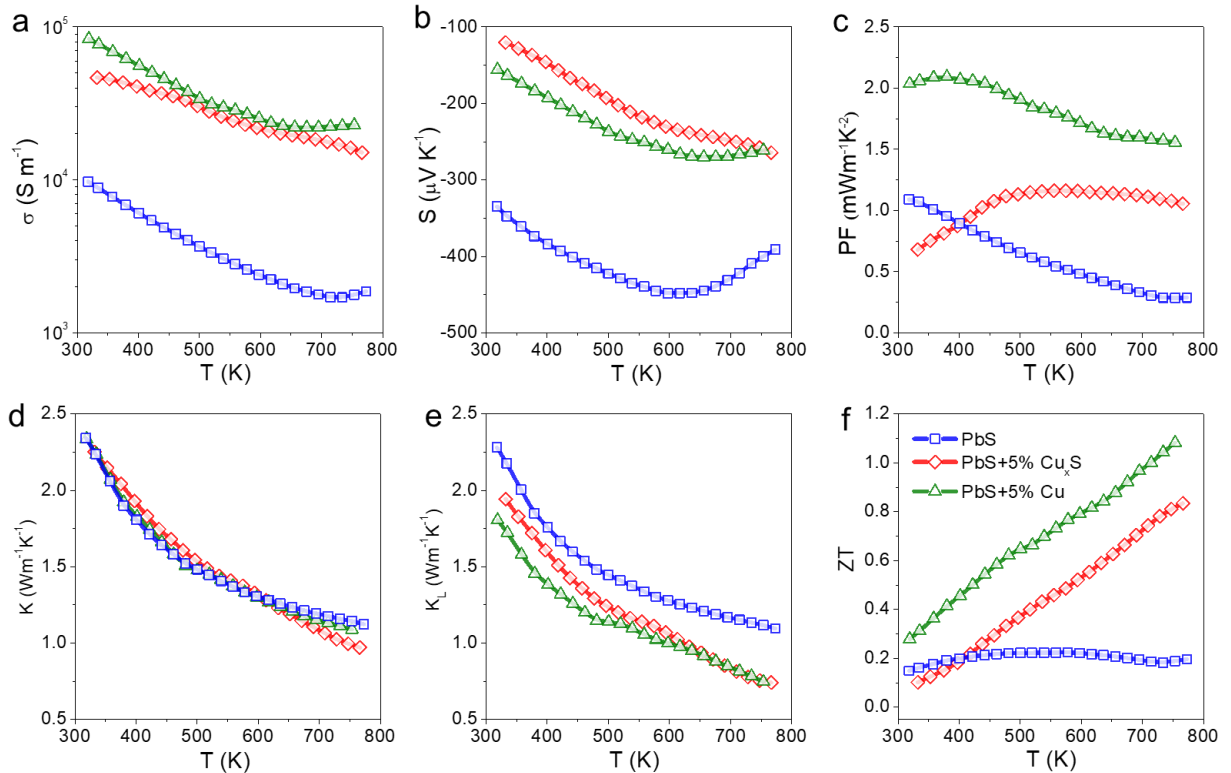


**Figure 7.** Comparison of the thermoelectric properties of the materials obtained from the consolidation of PbS nanoparticles, PbS nanoparticles combined with Cu<sub>x</sub>S nanoparticles and PbS nanoparticles combined with Cu particles: a) Electrical conductivity,  $\sigma$ ; b) Seebeck coefficient,  $S$ ; c) power factor,  $PF$ ; d) Thermal conductivity,  $\kappa$ ; e) Lattice thermal conductivity,  $\kappa_L$ . and e) Thermoelectric figure of merit,  $ZT$ .

## 4. Conclusion

We reported a facile, rapid, scalable and low-cost method for the synthesis of cubic PbS nanoparticles in aqueous media and at room temperature. The particles were annealed under a reducing atmosphere to remove surface PbO. The obtained powder was SPS sintered into high density pellets. The thermoelectric performance for n-type PbS was improved by blending the material with metallic Cu. The performance improvement was assigned to the presence of Pb domains generated by the reaction of Cu with S during the annealing process. The low work function of Pb enabled the Pb domains to inject charge into PbS, thus increasing the charge carrier concentration and the electrical conductivity. The large power factors obtained from these composites and the reduced lattice thermal conductivity over the whole temperature range resulted in high  $ZT$  value up to 1.1 at 750 K for PbS+5%Cu, which is about 4 times as high as that of undoped PbS. Besides, an average  $ZT_{ave}=0.72$  in the temperature range 320-773 K was demonstrated.

## 5. ASSOCIATED CONTENT

**Supporting Information.** The Supporting Information is available free of charge on the ACS Publications website. Additional characterization data including SEM, XRD, thermoelectric properties and literature comparison.

### Corresponding Author

\* Email: [yu.liu@ist.ac.at](mailto:yu.liu@ist.ac.at)

\* Email: [acabot@irec.cat](mailto:acabot@irec.cat)

### Author Contributions

The manuscript was written through the contributions of all authors. All authors have approved the final version of the manuscript.

### Notes

The authors declare no competing financial interest.

## 6. Acknowledgments

This work was supported by the European Regional Development Funds. MYL, YZ, XH, and KX thank the China Scholarship Council for scholarship support. M.I. has been financially supported by IST Austria and the Werner Siemens Foundation. Y.L. acknowledges funding from the European Union's Horizon 2020 research and innovation program under the Marie Skłodowska-Curie grant agreement No. 754411. J. Llorca is a Serra Húnter fellow and is grateful to ICREA Academia program and projects MICINN/FEDER RTI2018-093996-B-C31 and GC 2017 SGR 128. ICN2 acknowledges funding from Generalitat de Catalunya 2017 SGR 327 and the Spanish MINECO project NANOGEN (PID2020-116093RB-C43). ICN2 is supported by the Severo Ochoa program from Spanish MINECO (Grant No. SEV-2017-0706) and is funded by the CERCA Programme / Generalitat de Catalunya. X.H. thanks China Scholarship Council for scholarship support (201804910551). Part of the present work has been performed in the framework of Universitat Autònoma de Barcelona Materials Science PhD program.

## 7. References

- (1) Liu, Y.; Zhang, Y.; Lim, K. H.; Ibáñez, M.; Ortega, S.; Li, M.; David, J.; Martí-Sánchez, S.; Ng, K. M.; Arbiol, J.; et al. High Thermoelectric Performance in Crystallographically Textured N-Type  $\text{Bi}_2\text{Te}_{3-x}\text{Se}_x$  Produced from Asymmetric Colloidal Nanocrystals. *ACS Nano* **2018**, *12* (7), 7174–7184.
- (2) Liu, Y.; Zhang, Y.; Ortega, S.; Ibáñez, M.; Lim, K. H.; Grau-Carbonell, A.; Martí-Sánchez, S.; Ng, K. M.; Arbiol, J.; Kovalenko, M. V.; et al. Crystallographically Textured Nanomaterials Produced from the Liquid Phase Sintering of  $\text{Bi}_x\text{Sb}_{2-x}\text{Te}_3$  Nanocrystal Building Blocks. *Nano Lett.* **2018**, *18* (4), 2557–2563.
- (3) Zhang, Y.; Liu, Y.; Lim, K. H.; Xing, C.; Li, M.; Zhang, T.; Tang, P.; Arbiol, J.; Llorca, J.; Ng, K. M.; et al. Tin Diselenide Molecular Precursor for Solution-Processable Thermoelectric Materials. *Angew. Chemie* **2018**, *130* (52), 17309–17314.
- (4) Qin, Y.; Wang, D.; Hou, Z.; Xiao, Y.; Wang, G.; Huang, Z.; Zhao, L. D. Thermoelectric Transport Properties of PbS and Its Contrasting Electronic Band Structures. *Scr. Mater.* **2020**, *185*, 76–81.
- (5) Cheng, R.; Hao, S.; Li, J.; Bai, H.; Xie, S.; Gong, Y.; Liu, W.; Wu, J.; Tan, G.; Tang, X. Identifying the Origins of High Thermoelectric Performance in Group IIIA Element Doped PbS. *ACS Appl. Mater. Interfaces* **2020**, *12* (12), 14203–14212.
- (6) Wu, D.; Zhao, L. D.; Tong, X.; Li, W.; Wu, L.; Tan, Q.; Pei, Y.; Huang, L.; Li, J. F.; Zhu, Y.; et al. Superior Thermoelectric Performance in PbTe-PbS Pseudo-Binary: Extremely Low Thermal Conductivity and Modulated Carrier Concentration. *Energy Environ. Sci.* **2015**, *8* (7), 2056–2068.
- (7) Pei, Y.; Wang, H.; Snyder, G. J. Band Engineering of Thermoelectric Materials. *Adv. Mater.* **2012**, *24* (46), 6125–6135.
- (8) Luo, Z. Z.; Hao, S.; Cai, S.; Bailey, T. P.; Tan, G.; Luo, Y.; Spanopoulos, I.; Uher, C.; Wolverton, C.; Dravid, V. P.; et al. Enhancement of Thermoelectric Performance for N-Type PbS through Synergy of Gap State and Fermi Level Pinning. *J. Am. Chem. Soc.* **2019**, *141* (15), 6403–6412.
- (9) Liu, Y.; Calcabrini, M.; Yu, Y.; Lee, S.; Chang, C.; David, J.; Ghosh, T.; Spadaro, M. C.; Xie, C.; Cojocaru-Mirédin, O.; et al. Defect Engineering in Solution-Processed Polycrystalline SnSe Leads to High Thermoelectric Performance. *ACS Nano* **2021**.
- (10) Ibáñez, M.; Genç, A.; Hasler, R.; Liu, Y.; Dobrozhana, O.; Nazarenko, O.; De La Mata, M.; Arbiol, J.; Cabot, A.; Kovalenko, M. V. Tuning Transport Properties in Thermoelectric Nanocomposites through Inorganic Ligands and Heterostructured Building Blocks. *ACS Nano* **2019**, *13* (6), 6572–6580.
- (11) Ibáñez, M.; Luo, Z.; Genç, A.; Piveteau, L.; Ortega, S.; Cadavid, D.; Dobrozhana, O.; Liu, Y.; Nachtegaal, M.; Zebarjadi, M.; et al. High-Performance Thermoelectric Nanocomposites from Nanocrystal Building Blocks. *Nat. Commun.* **2016**, *7*, 1–7.

(12) Liu, Y.; Cadavid, D.; Ibáñez, M.; Ortega, S.; Martí-Sánchez, S.; Dobrozhana, O.; Kovalenko, M. V.; Arbiol, J.; Cabot, A. Thermoelectric Properties of Semiconductor-Metal Composites Produced by Particle Blending. *APL Mater.* **2016**, *4* (10), 104813.

(13) Hou, Z.; Qiu, Y.; Ren, D.; Huang, Z.; Zhao, L. D. Enhancing Thermoelectric Transport Properties of N-Type PbS through Introducing CaS/SrS. *J. Solid State Chem.* **2019**, *280*, 120995.

(14) Zhang, Y.; Xing, C.; Liu, Y.; Li, M.; Xiao, K.; Guardia, P.; Lee, S.; Han, X.; Ostovari Moghaddam, A.; Josep Roa, J.; et al. Influence of Copper Telluride Nanodomains on the Transport Properties of N-Type Bismuth Telluride. *Chem. Eng. J.* **2021**, *418*, 129374.

(15) Zhao, L. D.; He, J.; Hao, S.; Wu, C. I.; Hogan, T. P.; Wolverton, C.; Dravid, V. P.; Kanatzidis, M. G. Raising the Thermoelectric Performance of P-Type PbS with Endotaxial Nanostructuring and Valence-Band Offset Engineering Using CdS and ZnS. *J. Am. Chem. Soc.* **2012**, *134* (39), 16327–16336.

(16) Girard, S. N.; He, J.; Zhou, X.; Shoemaker, D.; Jaworski, C. M.; Uher, C.; Dravid, V. P.; Heremans, J. P.; Kanatzidis, M. G. High Performance Na-Doped PbTe-PbS Thermoelectric Materials: Electronic Density of States Modification and Shape-Controlled Nanostructures. *J. Am. Chem. Soc.* **2011**, *133* (41), 16588–16597.

(17) You, L.; Li, Z.; Ma, Q.; He, S.; Zhang, Q.; Wang, F.; Wu, G.; Li, Q.; Luo, P.; Zhang, J.; et al. High Thermoelectric Performance of Cu-Doped PbSe-PbS System Enabled by High-Throughput Experimental Screening. *Research* **2020**, *2020*, 1–8.

(18) Liu, B.; Ma, H.; Chen, Q.; Wang, Y.; Ji, G.; Li, X.; Zhang, Y.; Jia, X. Optimization and Modulation for the Moderate and High Temperature Thermoelectric Properties of PbSe via Solid Solution with PbS Synthesized by HPHT. *Mod. Phys. Lett. B.* **2020**, *34* (17), 1–9.

(19) Yu, L.; Maria, Ibáñez. Tidying Up the Mess. *Science*. **2021**, *371* (6530), 678–679.

(20) Qin, Y.; Xiao, Y.; Wang, D.; Qin, B.; Huang, Z.; Zhao, L. D. An Approach of Enhancing Thermoelectric Performance for P-Type PbS: Decreasing Electronic Thermal Conductivity. *J. Alloys Compd.* **2020**, *820*, 153453.

(21) Johnsen, S.; He, J.; Androulakis, J.; Dravid, V. P.; Todorov, I.; Chung, D. Y.; Kanatzidis, M. G. Nanostructures Boost the Thermoelectric Performance of PbS. *J. Am. Chem. Soc.* **2011**, *133* (10), 3460–3470.

(22) Hou, Z.; Wang, D.; Hong, T.; Qin, Y.; Peng, S.; Wang, G.; Wang, J.; Gao, X.; Huang, Z.; Zhao, L. D. Boosting Thermoelectric Performance of N-Type PbS through Synergistically Integrating In Resonant Level and Cu Dynamic Doping. *J. Phys. Chem. Solids* **2021**, *148*, 109640.

(23) Ibáñez, M.; Korkosz, R. J.; Luo, Z.; Riba, P.; Cadavid, D.; Ortega, S.; Cabot, A.; Kanatzidis, M. G. Electron Doping in Bottom-up Engineered Thermoelectric Nanomaterials through HCl-Mediated Ligand Displacement. *J. Am. Chem. Soc.* **2015**, *137* (12), 4046–4049.

(24) Yang, J.; Zhang, X.; Liu, G.; Zhao, L.; Liu, J.; Shi, Z.; Ding, J.; Qiao, G. Multiscale Structure and Band Configuration Tuning to Achieve High Thermoelectric Properties in N-Type PbS Bulks. *Nano Energy* **2020**, *74*, 104826.

(25) Jiang, B.; Liu, X.; Wang, Q.; Cui, J.; Jia, B.; Zhu, Y.; Feng, J.; Qiu, Y.; Gu, M.; Ge, Z.; et al. Realizing High-Efficiency Power Generation in Low-Cost PbS-Based Thermoelectric Materials. *Energy Environ. Sci.* **2020**, *13* (2), 579–591.

(26) Zhao, M.; Chang, C.; Xiao, Y.; Gu, R.; He, J.; Zhao, L. D. Investigations on Distinct Thermoelectric Transport Behaviors of Cu in N-Type PbS. *J. Alloys Compd.* **2019**, *781*, 820–830.

(27) Xiao, Y.; Wang, D.; Zhang, Y.; Chen, C.; Zhang, S.; Wang, K.; Wang, G.; Pennycook, S. J.; Snyder, G. J.; Wu, H.; et al. Band Sharpening and Band Alignment Enable High Quality Factor to Enhance Thermoelectric Performance in N-Type PbS. *J. Am. Chem. Soc.* **2020**, *142* (8), 4051–4060.

(28) Kowshik, M.; Vogel, W.; Urban, J.; Kulkarni, S. K.; Paknikar, K. M. Microbial Synthesis of Semiconductor PbS Nanocrystallites. *Adv. Mater.* **2002**, *14* (11), 815–818.

(29) Li, Y.; Lin, J.; Xie, H.; Wang, Y.; Li, Z. Raising the Thermoelectric Performance of PbS with Low-Content Polyparaphenylene. *J. Mater. Sci. Mater. Electron.* **2020**, *31* (9), 6586–6592.

(30) Calcabrini, M.; Genç, A.; Liu, Y.; Kleinhanns, T.; Lee, S.; Dirin, D. N.; Akkerman, Q. A.; Kovalenko, M. V.; Arbiol, J.; Ibáñez, M. Exploiting the Lability of Metal Halide Perovskites for Doping Semiconductor Nanocomposites. *ACS Energy Lett.* **2021**, *6* (2), 581–587.

(31) Zhao, L.; Yang, J.; Lu, B.; Zhang, X.; Hu, J.; Xie, W.; Shao, H.; Liu, G.; Hussain, S.; Shi, Z.; et al. Enhanced Thermoelectric Properties of N-Type Cl Doped PbS-Based Materials via Bi Alloying. *J. Alloys Compd.* **2020**, 157788.

(32) Li, M.; Liu, Y.; Zhang, Y.; Han, X.; Zhang, T.; Zuo, Y.; Xie, C.; Xiao, K.; Arbiol, J.; Llorca, J.; et al. Effect of the Annealing Atmosphere on Crystal Phase and Thermoelectric Properties of Copper Sulfide. *ACS Nano* **2021**, *15* (3), 4967–4978.

(33) Kim, H. S.; Gibbs, Z. M.; Tang, Y.; Wang, H.; Snyder, G. J. Characterization of Lorenz Number with Seebeck Coefficient Measurement. *APL Mater.* **2015**, *3* (4), 1–6.

(34) Burungale, V. V.; Devan, R. S.; Pawar, S. A.; Harale, N. S.; Patil, V. L.; Rao, V. K.; Ma, Y. R.; Ae, J. E.; Kim, J. H.; Patil, P. S. Chemically Synthesized PbS Nanoparticulate Thin Films for a Rapid NO<sub>2</sub> Gas Sensor. *Mater. Sci. Pol.* **2016**, *34* (1), 204–211.

(35) Koch, V. M.; Barr, M. K. S.; Büttner, P.; Mínguez-Bacho, I.; Döhler, D.; Winzer, B.; Reinhardt, E.; Segets, D.; Bachmann, J. A Solution-Based ALD Route towards (CH<sub>3</sub>NH<sub>3</sub>)(PbI<sub>3</sub>) Perovskite: Via Lead Sulfide Films. *J. Mater. Chem. A* **2019**, *7* (43), 25112–25119.

(36) Zuo, Y.; Liu, Y.; Li, J.; Du, R.; Han, X.; Zhang, T.; Arbiol, J.; Divins, N. J.; Llorca, J.;

Guijarro, N.; et al. In Situ Electrochemical Oxidation of  $\text{Cu}_2\text{S}$  into  $\text{CuO}$  Nanowires as a Durable and Efficient Electrocatalyst for Oxygen Evolution Reaction. *Chem. Mater.* **2019**, *31* (18), 7732–7743.

(37) Liu, Y.; Zhang, Y.; Lim, K. H.; Ibáñez, M.; Ortega, S.; Li, M.; David, J.; Martí-Sánchez, S.; Ng, K. M.; Arbiol, J.; et al. High Thermoelectric Performance in Crystallographically Textured n Type  $\text{Bi}_{2}\text{Te}_{3-x}\text{Se}_x$  Produced from Asymmetric Colloidal Nanocrystals. *ACS Nano* **2018**, *12*, 7174–7184.

(38) Zhang, Y.; Xing, C.; Liu, Y.; Spadaro, M. C.; Wang, X.; Li, M.; Xiao, K.; Zhang, T.; Guardia, P.; Lim, K. H.; et al. Doping-Mediated Stabilization of Copper Vacancies to Promote Thermoelectric Properties of  $\text{Cu}_{2-x}\text{S}$ . *Nano Energy* **2021**, *85*, 105991.

(39) Qin, B.; He, W.; Zhao, L. D. Estimation of the Potential Performance in P-Type SnSe Crystals through Evaluating Weighted Mobility and Effective Mass. *J. Mater.* **2020**, *6* (4), 671–676.

(40) Pan, L.; Mitra, S.; Zhao, L. D.; Shen, Y.; Wang, Y.; Felser, C.; Berardan, D. The Role of Ionized Impurity Scattering on the Thermoelectric Performances of Rock Salt  $\text{AgPb}_m\text{SnSe}_{2+m}$ . *Adv. Funct. Mater.* **2016**, *26* (28), 5149–5157.

(41) Serrano, T.; Gómez, I. One Pot Synthesis of  $\text{PbS}/\text{Cu}_2\text{S}$  Core-Shell Nanoparticles and Their Optical Properties. *Rev. Mex. Fis.* **2014**, *60* (1), 14–21.

## TOC graphical abstract

